# The Surprising *in Vivo* Instability of Near-IR-Absorbing Hollow Au−Ag Nanoshells

Amanda M. Goodman,[†] Yang Cao,[‡] Cordula Urban,[‖] Oara Neumann,[‡,§] Ciceron Ayala-Orozco,[†] Mark W. Knight,[§] Amit Joshi,[‖] Peter Nordlander,[‡,§] and Naomi J. Halas[†,‡,§,⊥,*]

[†]Department of Chemistry, [‡]Department of Physics and Astronomy, [§]Department of Electrical and Computer Engineering, and [⊥]Department of Bioengineering, Rice University, Houston, Texas 77005, United States, and [‖]Department of Radiology, Baylor College of Medicine, Houston, Texas 77030, United States

ABSTRACT Photothermal ablation based on resonant illumination of near-infrared-absorbing noble metal nanoparticles that have accumulated in tumors is a highly promising cancer therapy, currently in multiple clinical trials. A crucial aspect of this therapy is the nanoparticle size for optimal tumor uptake. A class of nanoparticles known as hollow Au (or Au−Ag) nanoshells (HGNS) is appealing because near-IR resonances are achievable in this system with diameters less than 100 nm. However, in this study, we report a surprising finding that *in vivo* HGNS are unstable, fragmenting with the Au and the remnants of the sacrificial Ag core accumulating differently in various organs. We synthesized 43, 62, and 82 nm diameter HGNS through a galvanic replacement reaction, with nanoparticles of all sizes showing virtually identical NIR resonances at ∼800 nm. A theoretical model indicated that alloying, residual Ag in the nanoparticle core, nanoparticle porosity, and surface defects all contribute to the presence of the plasmon resonance at the observed wavelength, with the major contributing factor being the residual Ag. While PEG functionalization resulted in stable nanoparticles under laser irradiation in solution, an anomalous, strongly element-specific biodistribution observed in tumor-bearing mice suggests that an avid fragmentation of all three sizes of nanoparticles occurred *in vivo*. Stability studies across a wide range of pH environments and in serum confirmed HGNS fragmentation. These results show that NIR resonant HGNS contain residual Ag, which does not stay contained within the HGNS *in vivo*. This demonstrates the importance of tracking both materials of a galvanic replacement nanoparticle in biodistribution studies and of performing thorough nanoparticle stability studies prior to any intended *in vivo* trial application.
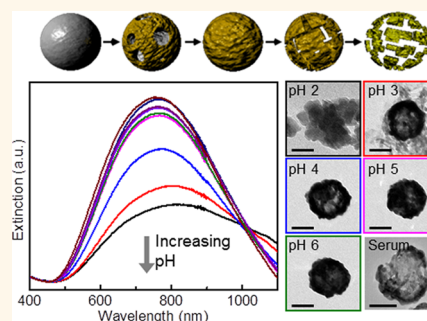
KEYWORDS: plasmon · fragmentation · serum · near-infrared · photothermal therapy · nanomedicine · cancer

Cancer is one of the most devastating diseases facing the human population. There is currently intense interest in engineering nanoparticles for diagnosis and/or treatment of this disease.[1−3] In particular, photothermal therapy (PTT) has emerged as an effective way to selectively ablate tumors. When nanoparticles are taken up into tumors, the tumor is irradiated with near-infrared (NIR) light at the nanoparticle plasmon resonance. The absorbed light is converted into heat, resulting in cell hyperthermia, subsequent cell death, and tumor remission.[1−3] Because of the low inherent absorption of NIR light in tissue, the light itself does not significantly damage the tissue in the absence of nanoparticles, rendering this approach minimally invasive.[4] Photothermal therapy has been successfully demonstrated with many NIR-absorbing gold nanostructures including silica−gold nanoshells,[2,5,6] nanorods,[7−9] branched nanoparticles,[10] nanohexapods,[11] nanocages,[12,13] and hollow gold nanoshells.[14,15]

It is widely believed that passive (non-antibody-targeted) uptake of nanoparticles in cells and in tumors is dependent upon nanoparticle size, in addition to other factors such as zeta potential, and should be enhanced for nanoparticles with sizes below 100 nm. For example, 45 nm gold nanoparticles have been shown with optical sectioning microscopy to have higher uptake in lung cancer and HeLa cells than 70 and 100 nm gold nanoparticles.[16] Passive uptake in tumors is known as the enhanced permeability and retention (EPR) effect and occurs due to the leaky vasculature and poor lymphatic drainage characteristic of

tumors.[17,18] Hollow core—shell nanoparticles, whose internal geometry can be adjusted to achieve strong NIR absorption across a broad particle size range, can provide this property in the sub-100 nm nanoparticle size range.

Multiple groups have reported that hollow Au nanoshells (HGNS) can be made successfully in the sub-100 nm size range, with NIR plasmon resonances, using a galvanic replacement reaction between Au and Ag, or Au and Co.[19−26] In a galvanic replacement synthesis, a salt solution of a given metal with a high reduction potential is added to a colloidal solution of a metal with a lower reduction potential. The difference in reduction potentials causes the metal in the salt solution to be reduced, while the metal in the nanoparticle template simultaneously oxidizes. For the case of Au and Ag, the galvanic replacement occurs according to the following reaction.[27]

$$3Ag(s) + AuCl_4^-(aq) \rightarrow Au(s) + 3Ag^+(aq) + 4Cl^-(aq)$$
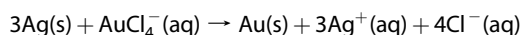
The standard reduction potential of the $AuCl_4^-$/Au pair is 0.99 V vs standard hydrogen electrode (SHE) compared to 0.80 V vs SHE for Ag^+/Ag.[27] Xia and co-workers have shown that, by starting with Ag cubes, NIR sub-100 nm Au nanocages can be formed by galvanic replacement and subsequently show applicability for biomedical applications.[28] Following this work, HGNS were synthesized using sacrificial Co cores[22,29−31] and have also shown potential for biomedical applications.[14,15,32−35] However, the $in vivo$ stability of HGNS has not been well studied, and to our knowledge, published biodistribution studies have focused on only the shell material. The fate of the sacrificial core material has yet to be investigated in this context.

Here we show that HGNS with sizes varying from 43 to 82 nm in diameter can be synthesized using sacrificial Ag cores, with virtually identical NIR resonances across this size range. We examined the NIR resonance properties of this nanoparticle in detail including the use of theoretical simulations, where we observed that alloying of the two constituent metals, porosity of the remnant sacrificial layer, and the presence of surface defects all play an important role in determining the plasmon resonance frequency and line width. We investigated the stability of the nanoparticles before and after functionalization with polyethylene glycol (PEG) under laser irradiation, preliminarily to $in vivo$ studies. We then performed biodistribution studies of the HGNS nanoparticles in mice. Here we made the unexpected observation that the constituent metals of the nanoparticle have dramatically different biodistribution profiles. To better understand the origin of this variation in biodistribution, nanoparticle stability was investigated across a range of pH environments and in human serum at physiological pH. In serum and in strong pH environments, the structural integrity of the
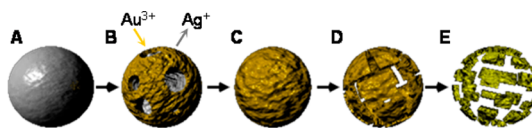
Scheme 1. Schematics showing the synthesis of HGNS by galvanic replacement. (A) Starting with Ag colloid, $AuCl_3$ is added, causing (B) Ag to oxidize and Au^{3+} ions to simultaneously reduce. (C) As the replacement continues, mass flows from the central region of the nanoparticle, forming a complete HGNS. (D) Then, dealloying occurs, resulting in fragmentation of the nanoparticle shell. (E) After complete Ag oxidation and diffusion, only pure Au fragments remain

nanoparticles is strongly compromised. Our results indicate that disintegration of HGNS nanoparticles $in vivo$ may quite possibly be a common occurrence. Therefore, careful characterization of multicomponent particles needs to be thoroughly pursued prior to any planned $in vivo$ application.

RESULTS AND DISCUSSION

Synthesis of HGNS. HGNS were synthesized with sacrificial Ag cores through a galvanic replacement reaction (Scheme 1). The reaction starts with the oxidation of Ag colloid (Scheme 1A) through the formation of pinholes. Since an Au/Ag alloy is more thermodynamically stable than either of the pure metals, as Au reduces on the surface of the Ag nanoparticle, a thin, incomplete alloy shell forms (Scheme 1B).[36] The oxidation of the Ag continues through the pinholes and empties the central region of the nanoparticle via the Kirkendall effect. Net mass flow toward the shell occurs because Ag diffuses faster into Au than $vice versa$.[20,21,28] The shell then reshapes, with the pinholes reducing in size through Ostwald ripening (Scheme 1C).[27] At this stage, Ag is still present in the nanoparticle. Next, dealloying occurs (Scheme 1D). The dealloying process produces many holes, since each Au atom replaces three Ag atoms. The Ag is fully oxidized once the dealloying process has transformed the nanoparticle into smaller components composed of pure Au (Scheme 1E). In fact, pinhole-free particles were found to commonly retain ~30% of their initial Ag content.[36] The pinhole-free HGNS exhibit a plasmon resonance located at 634 nm for a diameter of 50 nm.[27]

Three different diameters (40, 60, and 80 nm) of Ag cores were used. By adding a solution of gold chloride and potassium carbonate to a colloidal suspension of the Ag nanoparticles, HGNS of 82.6 ± 4.2, 61.8 ± 3.3, and 43.1 ± 3.9 nm were formed. Figure 1A shows the extinction spectra of the Ag colloid (top panel) and the HGNS (bottom panel), and corresponding transmission electron microscopy (TEM) images are shown in Figure 1B and C.

The optical signature of HGNS formation was studied and then correlated with its structural and compositional evolution during growth. After adding the $AuCl_3$ solution, HGNS with a resonance at ~820 nm

were formed. Over time, Ag continued to be oxidized from the core, as Au^{3+} continued to be reduced. As the
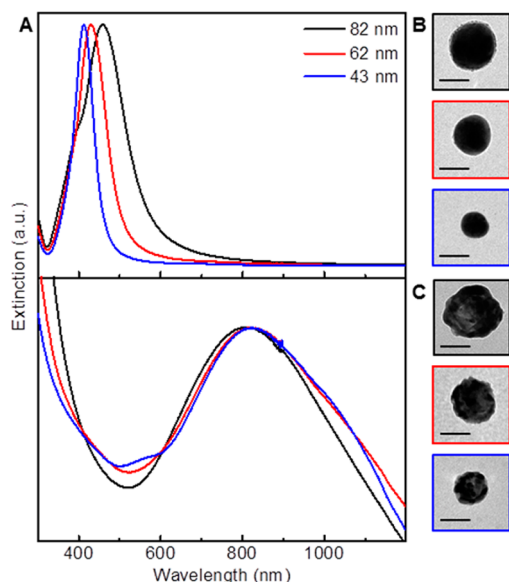
Figure 1. Extinction spectra and TEM images of Ag nanoparticle precursors and HGNS. (A) Extinction spectra of Ag colloid with 80, 60, and 40 nm diameters (top panel) and resulting HGNS of 82, 62, and 43 nm diameters (bottom panel). Representative TEM images of (B) 80, 60, and 40 nm Ag colloids and (C) 82, 62, and 43 nm HGNS are shown. All scale bars are 50 nm.

ratio of Ag:Au decreased, there was an accompanying blue-shift of the plasmon resonance (Figure S1). Using X-ray photoelectron spectroscopy (XPS), the atomic percent of Ag and Au at various reaction times was determined (Figure S2). At early reaction times of an 82 nm HGNS, the ratio of Ag to Au was high, 4:1. However, if the reaction was allowed to proceed for 24 h, that ratio was reduced to ~1:1 and the plasmon resonance shifted to the visible region. Given the desire to produce NIR-active HGNS, for all further experiments, HGNS were allowed to react for only 1 h, which resulted in NIR resonances and a corresponding Ag:Au ratio of 4:1.

Theoretical Modeling. Calculations based on the finite element method (COMSOL) were performed to better understand the origin of the NIR resonance in this family of nanoparticles and to provide further insight into their structural composition prior to *in vivo* studies. Experimentally determined dielectric functions for both Au and Ag were used (see Supporting Information).[37] Based on our theoretical modeling, for the nanoparticle to support a plasmon resonance in the NIR, it must have a structure similar to that shown in Scheme 1B, where the nanoparticle shell is composed of Au/Ag alloy with multiple large defects on its surface (Figure 2A, inset SEM image). Because three Ag atoms are removed for every Au atom added, the metallic
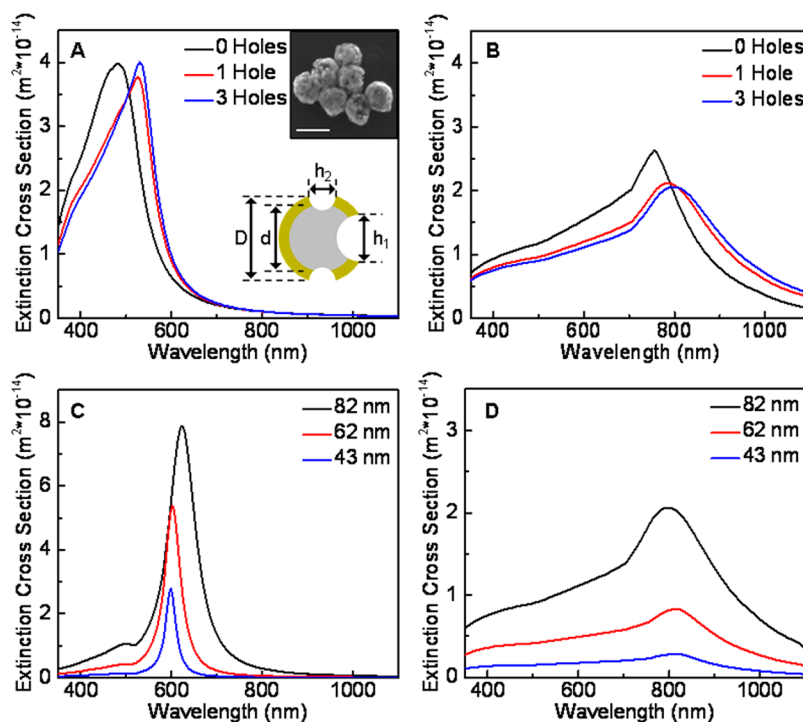
Figure 2. Finite element method (FEM) modeling and Mie theory of HGNS showing the influence of material porosity on the plasmon properties. Extinction cross sections calculated with the FEM of 82 nm diameter HGNS comparing the presence of holes in the particle surface with (A) nonporous (80% Ag, 20% Au) and (B) porous materials (43.2% Ag, 10.8% Au, and 46% H$_2$O). Spectra are plotted for the average E field polarization. (C) Extinction cross section spectra of the three sizes of HGNS with a H$_2$O core, alloy shell, and zero holes calculated with Mie theory show similar plasmon resonances in the visible region. (D) The three-hole porous model is used to calculate with FEM the extinction cross section spectra of 82, 62, and 43 nm diameter HGNS with extinction maxima of 800, 815, and 815 nm, respectively.

alloy and core must be porous. To account for the corresponding modification to the metallic dielectric functions that this compositional change would induce, simulations were performed where the HGNS was modeled as a spherical, porous silver core coated with a similarly porous Au/Ag alloy shell. The porous materials were modeled using the Bruggeman effective medium theory.[38]

The Bruggeman effective medium theory has been widely used to obtain effective material parameters for two dissimilar, porous materials.[39] The Bruggeman effective approximation formula can be written as[38,40]

$$f_1 \frac{\varepsilon_1 - \varepsilon_{\text{eff}}}{\varepsilon_{\text{eff}} + g(\varepsilon_1 - \varepsilon_{\text{eff}})} + (1 - f_1) \frac{\varepsilon_2 - \varepsilon_{\text{eff}}}{\varepsilon_{\text{eff}} + g(\varepsilon_2 - \varepsilon_{\text{eff}})} = 0$$

where ε_1 and ε_2 are the complex dielectric functions of the constituent materials. The coefficient f_1 represents the volume fraction of one material in the composite, with the remaining material comprising a fill fraction of $(1 - f_1)$. The constant g is a geometric factor; for spherical inclusions $g = 1/3$. In the case of porous Ag, the effective dielectric is calculated as a compositional mixture of Ag with H_2O. To obtain an effective dielectric for the porous alloy, a more general form of the Bruggeman effective model is used, to include more than two different composite materials (*i.e.*, Ag, Au, and H_2O):

$$\sum_i f_i \frac{\varepsilon_i - \varepsilon_{\text{eff}}}{\varepsilon_{\text{eff}} + g(\varepsilon_i - \varepsilon_{\text{eff}})} = 0$$

Now $i = 3$, and ε_i and f_i are the complex dielectric function and the volume fraction of the ith constituent material, respectively.[41] The above equation yields a unique physical solution for ε_{eff} in the absence of gain.

To investigate the role of the nanoporous alloy in determining the plasmon resonance properties, the nanoparticle geometries, with their constituent materials, were simulated independently as being composed of either a nonporous or porous medium and compared to nanoparticles simulated with H_2O cores. The nanoparticles were also simulated with zero, one, and three holes to isolate the influence of shell defects on peak position. For an asymmetric nanoparticle, the extinction cross section can depend upon the orientation of the particle relative to the polarization of incident light. To account for this, the nanoparticles were simulated with the E field polarized in the x, y, and z directions independently, then averaged; for the spectra shown in Figure 2, the average of all three polarizations is shown. All nanoparticles were simulated with a background medium of H_2O. The inset in Figure 2A illustrates the geometry of the model used, where d is the diameter of the core and D is the outer diameter including the shell. To emulate the large holes in the surface of the HGNS, the modeled geometry included three spherical holes: one large hole with a diameter of h_1 and two smaller holes each with diameter h_2. The parameters used for each particle

size are listed in Table S1 (Supporting Information). The simulations showed that the presence of holes of either large or small diameter has a minimal effect on the plasmon resonance.

The case of a nonporous HGNS with an 82 nm diameter, a solid Ag core, and a solid Ag/Au alloy shell is shown in Figure 2A. For this structure, the plasmon resonance peak wavelength occurs at $\lambda = 480$ nm, far from our experimentally observed resonance. The introduction of defects into the shell layer red-shifts the plasmon resonance slightly, but only by $\sim$50 nm (Figure 2A). However, when porosity is introduced, it induces a much larger red-shift of the plasmon resonance, by 275 nm (Figure 2B). The addition of large surface defects also results in an additional red-shift of the plasmon resonance, to a wavelength region corresponding to our experimental observations, nominally 800 nm (Figure 2B). The dielectric functions used to calculate Figure 2A and Figure 2B for the nonporous and porous materials, respectively, are shown in Figure S3.

The role of porosity is further emphasized by comparing the porous nanoparticle simulations to simulations of the three sizes of HGNS with pure H_2O cores, which is the expected composition for HGNS (Figure 2C). In this case, Mie theory was used to simulate the shell as a continuous alloy composed of 80% Ag and 20% Au with the dimensions listed in Table S1. The inside core and background media are H_2O. The core to shell ratio for each particle size is $\sim$0.8, and as a result, their plasmon resonances are expected to be similar. Interestingly, when the nonporous nanoparticles are hollow, their plasmon resonances are only at $\sim$600 nm. This set of simulations demonstrates that it is highly likely that all three factors of (1) alloying, (2) porosity, and (3) surface defects contribute, in concert, to the NIR resonances observed in the solution phase absorption spectrum of the HGNS, but that the presence of a porous Ag core is required to shift the plasmon to the NIR.

The degree of porosity of the constituent materials of the nanoparticle also strongly affects the plasmon peak position. Using the three-defect porous HGNS model geometry, the percentage of H_2O (*i.e.*, the porosity) in the nanoparticle was gradually increased. This increase introduces a significant red-shift of the plasmon resonance: by varying the porosity from 40% to 46%, an additional shift of the plasmon resonance from 660 nm to 800 nm is obtained (Figure S4).

Figure 2D shows the average polarization spectrum for each of the three sizes of HGNS. The extinction maxima for the averaged spectra are 800, 815, and 815 nm, and the percentages of water are 46%, 46.3%, and 46.4% for 82, 62, and 43 nm HGNS, respectively. Because the percentage of H_2O in the nanoparticle cannot be determined experimentally, the H_2O composition was determined theoretically by the percent required to achieve the desired plasmon resonance.

TABLE 1. Extinction Maximum and Zeta Potential of 80, 60, and 40 nm Diameter Ag Colloids and the Corresponding HGNS and HGNS@PEG

particle type	80 nm		60 nm		40 nm	
	extinction max (nm)	zeta potential (mV)	extinction max (nm)	zeta potential (mV)	extinction max (nm)	zeta potential (mV)
Ag colloid	458	-49.7 ± 2.2	430	-48.6 ± 1.0	412	-46.9 ± 0.9
HGNS	811	-30.6 ± 0.2	826	-35.2 ± 0.6	825	-41.7 ± 1.0
HGNS@PEG	804	-12.3 ± 0.1	806	-11.1 ± 0.2	787	-9.8 ± 1.6
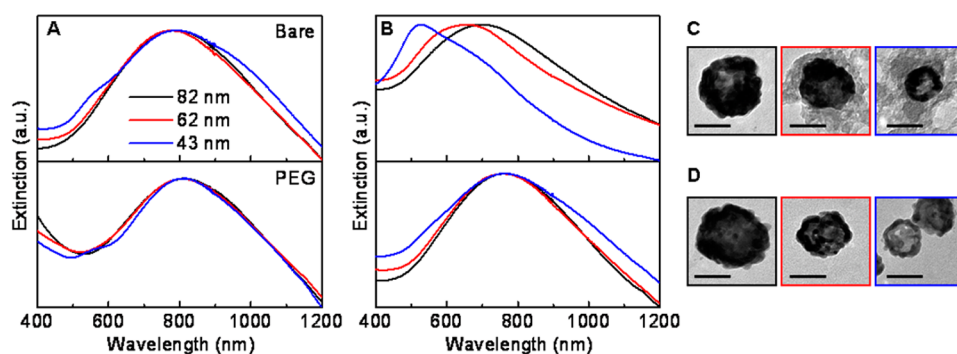
Figure 3. Effect of laser irradiation on HGNS with an 800 nm CW laser at 2.0 W/cm² for 25 min for three diameters: 82 nm (black), 62 nm (red), and 43 nm (blue). Extinction spectra of HGNS (top panel) and HGNS@PEG (bottom panel) (A) before and (B) after laser irradiation. TEM images of 82, 62, and 43 nm diameter (C) HGNS and (D) HGNS@PEG after laser irradiation. All scale bars are 50 nm.

Surface Functionalization. For biological applications, the HGNS need to be functionalized with polyethylene glycol (PEG). Coating the particles in PEG is important for several reasons.[13,17,42,43] First, PEGylation improves circulation time of the nanoparticles *in vivo*.[42,43] Second, it inhibits opsonization, the process by which foreign structures such as nanoparticles are identified for endocytosis by phagocytes.[17,42,43] Third, PEGylation allows the surface charge of the particles to be reduced to near neutrality, since highly charged nanoparticles have shown increased accumulation in the reticuloendothelial system (liver and spleen).[17,18]

The HGNS were functionalized with PEG in two steps to achieve a zeta potential of approximately −10 mV, appropriate for tumor uptake studies *in vivo*. The HGNS were first coated with 10 000 MW thiol-mPEG (thiol-PEG-methyl), then subsequently with 10 000 MW thiol-PEG-amine using a warm water bath to increase the packing density without furthering Ag oxidation. The two-step coating allowed the zeta potential to be reduced to about −10 mV, while avoiding a highly positively charged surface that would have resulted from thiol-PEG-amine alone. In contrast, one-step coating with thiol-mPEG alone only reduced the highly negative zeta potential of the bare HGNS to about −23 mV. The unusual high negative zeta potential observed for HGNS@mPEG supports the idea that the surface is indeed composed of an alloy of Au and Ag, since mPEG thiolation of Au nanoparticles typically results in a much lower zeta potential than we observe for the uncoated nanoparticles. Table 1 shows the extinction maximum and zeta

potentials of the Ag colloid precursor, HGNS, and HGNS@PEG for the three particle core sizes. After PEGylation, the HGNS retain their similar plasmon resonances.

NIR Laser Irradiation. A primary application for chemically synthesized NIR-active particles is photothermal therapy. HGNS are desirable for photothermal therapy because their thinner shells have a low thermal mass, which should enable efficient heat dissipation to the surrounding tissues.[22] The effect of laser irradiation was tested on solutions of bare and PEGylated HGNS (Figure 3). The nanoparticles were irradiated with a continuous wave 800 nm diode laser at 2.0 W/cm² for 25 min. Figure 3A shows the extinction spectra before irradiation, and Figure 3B shows the extinction after irradiation. After irradiation, there is a drastic size-dependent blue-shift of the plasmon resonance of the bare HGNS, with the smallest nanoparticles being affected most dramatically. The TEM images reveal that the bare nanoparticles have changed in morphology and have also likely leached Ag into the solution (Figure 3C). Alternatively, the HGNS@PEG extinction spectra are stable after irradiation and the TEM images confirm that the HGNS@PEG remain intact (Figure 3D). These results suggested that HGNS@PEG would be viable nanoparticles for photothermal therapy.

Biodistribution. Here, the three sizes of HGNS were PEGylated for *in vivo* studies in nine mice, with three mice for each nanoparticle size. Nanoparticles were injected into the tail vein of nude mice, each with a glioma xenograft transplanted from a U87 cell line. The mice were sacrificed 24 h postinjection. The biodistribution of the
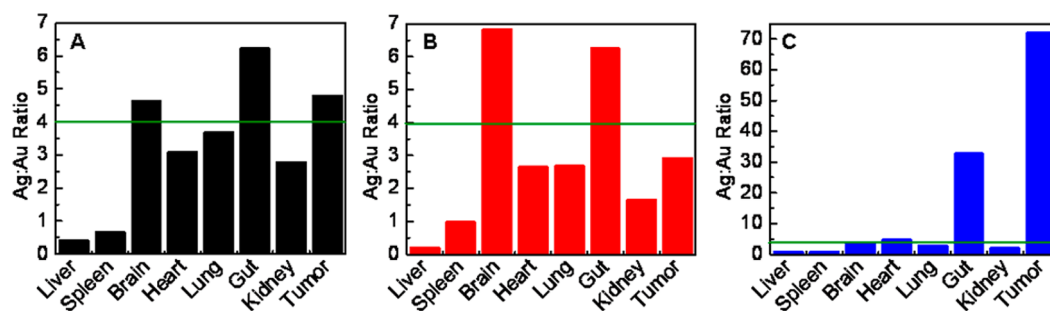
Figure 4. Comparison of the Ag:Au ratio in each organ determined by ICP-MS for 82 (A), 62 (B), and 43 nm diameter HGNS@PEG (C). Ag and Au content were calculated in μg/g of organ. The green line indicates the expected Ag:Au ratio of 4:1 as determined by XPS analysis of the particles prior to injection.
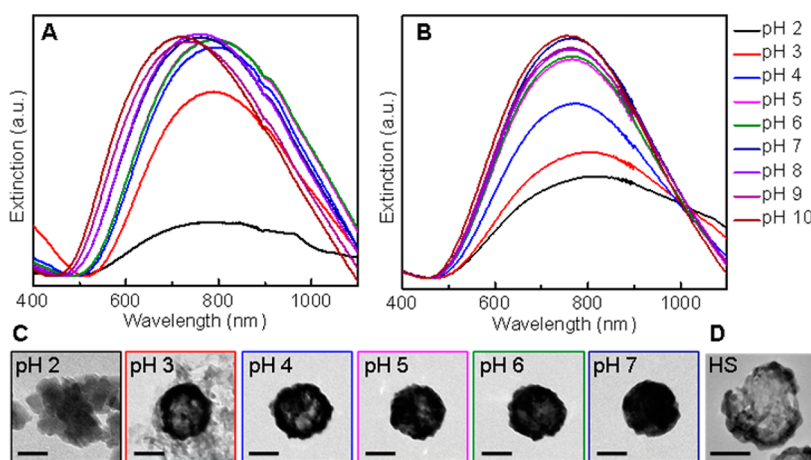

Figure 5. Effect of a range of pH and human serum on HGNS with and without PEG. Extinction spectra of 82 nm diameter HGNS (A) and HGNS@PEG (B) after 24 h incubation in water adjusted to various pH. (C) TEM images of HGNS@PEG after 24 h incubation at pH 2−7. (D) HRTEM image of HGNS@PEG after 24 h incubation in human serum at physiological pH. All scale bars are 50 nm.

HGNS was examined by inductively coupled plasma mass spectrometry (ICP-MS) to quantify the Ag and Au content in each organ (Figure S5). The error bars in Figure S5A represent the standard deviation of Au content in each organ for the three mice injected with HGNS of 82, 62, or 43 nm. Error bars in Figure S5B were calculated in the same manner for Ag content. For all nanoparticle sizes, there is a high uptake in the liver and spleen, which is common and has been observed by other groups.[42,44,45] Notably, however, there is a variable ratio of Ag:Au in each organ. The average Ag:Au ratio was determined for each nanoparticle size and is shown in Figure 4. Assuming that the particles have a ratio of 4:1 Ag:Au (as determined by XPS), it would be expected in each organ to find three times more Ag than Au. However, the ratio varies considerably between organs. In fact, in the liver and spleen the Au content is actually higher than the Ag content. The variable ratio of Ag:Au in each organ indicates that the particles are fragmenting at some point after injection. Furthermore, data from Figure 3 suggest that the fragmentation of the particles is size dependent. The 43 nm HGNS shows a very large amount of Ag surrounding the particle after laser irradiation. As the overall particle size decreases, the shell becomes thinner. This thinner shell allows the 43 nm particle to fragment quicker, leading to

the more drastic variation in Au and Ag distribution seen in mice injected with the 43 nm HGNS. For biological applications it is imperative that the Ag be unaffected by the environment and stay confined within the particles, due to potential cytotoxic effects.[46−48]

Stability Studies. To explain the fragmentation of the HGNS *in vivo*, stability studies were performed on the 82 nm HGNS in a range of pH and in serum. *In vivo*, the nanoparticles are subjected to a range of pH values as they traffic throughout the organism;[49] therefore, we first investigated their pH stability. The 82 nm HGNS were dispersed in aqueous solutions with pH ranging from 2 to 10 for 24 h, and the extinction spectrum of the nanoparticles was monitored for changes resulting from each environment. When bare 82 nm diameter HGNS were incubated in various pH solutions, a large shift of the plasmon resonance from 805 to 712 nm was observed (Figure 5A). With HGNS@PEG, we observe a large shift of the plasmon resonance from 811 to 769 nm from pH 2−4, but only a small shift from from 769 to 756 nm for pH 4−10 (Figure 5B). This suggests that PEG cannot protect the particles in acidic pH. In both cases, we see a decrease in the extinction at low pH, suggesting aggregation or breakdown of nanoparticles. TEM images of HGNS@PEG incubated in pH 2−7

for 24 h reveal that the particles are in fact destroyed at low pH (Figure 5C).

Within physiological environments, the nanoparticles are exposed to many other factors in addition to various pH environments. In order to simulate a complex biological environment, the HGNS were dispersed in serum at physiological pH. Serum is the portion of the blood that does not contain the blood cells, platelets, or fibrinogens. However, it does contain dissolved gases such as oxygen and carbon dioxide, proteins including albumin and antibodies, as well as antigens, salts such as sodium, chloride, and potassium ions, hormones, oligonucleotides, etc.[50,51] The HGNS@PEG were incubated in human serum for 24 h, and high-resolution transmission electron microscope (HRTEM) images were taken to investigate the structural integrity of HGNS in the in vivo-like environment. The HRTEM image reveals that the particles break apart in serum at physiological pH, similarly to the nanoparticle fragmentation observed at low pH (Figure 5D). The particles were also incubated in fetal bovine serum, which showed fragmentation of the particles as well (TEM not shown).

It is probable that the cause of the destruction of the particles originates with the presence of Ag on the surface of the nanoparticles. Many studies have shown the instability of Ag nanoparticles.[52] Lok et al. demonstrated Ag nanoparticle aggregation in media with high ionic strength.[53] Bouwmeester et al. showed that Ag nanoparticles incubated in cell culture media dissociated into Ag ions,[54] and Stebounova et al. showed that Ag nanoparticles aggregate in artificial interstitial and lysosomal fluid with only 1% of particles remaining suspended after 24 h.[55] Moreover, Hurt and co-workers have shown pH-dependent dissolution of Ag nanoparticles, with higher degrees of Ag dissolution occurring at lower pH.[49,56] Most notably, Hurt and co-workers concluded that dissolved O_2 in solution is crucial for Ag dissolution.[56] In deoxygenated acetate buffer at pH 4, Ag dissolution is negligible, but it is drastically increased in air-saturated acetate buffer at pH 4. The protons and dissolved O_2 cooperatively oxidize the Ag. In the case of HGNS, dissolved O_2 is present in all solutions, resulting in some degree of oxidation; but as the pH is decreased, more protons are available to cooperatively oxidize the Ag in the shell layer, and subsequently at very low pH Ag from the core is oxidized, destroying the integrity of the HGNS.

Another factor potentially influencing stability is the protein corona that immediately forms on the surface of nanoparticles when introduced in vivo.[57] Any one of the more than 3700 proteins in plasma[58]

could have a degradative effect on the nanoparticles. However, because biological media are so complex, it is difficult to deduce one specific cause of HGNS fragmentation; instead, it is likely that a variety of factors in this complex environment contribute to the fragmentation, including high ionic strengths, proteins, low pH environments, and dissolved O_2.[49,53,55−57]

This study shows that it is critically important that the remnant sacrificial core material and the shell material of HGNS both be monitored independently when performing biodistribution studies. The results shown here indicate that, although this nanoparticle family has a highly promising set of characteristics for in vivo use, it may be substantially degraded in vivo even when PEGylated. Consequently, further investigation into the fragmentation and toxicity of HGNS is necessary to determine their ultimate suitability for nanomedical applications.

CONCLUSION

HGNS of three sizes below 100 nm in diameter were synthesized with plasmon resonances in the NIR region as potential photothermal transducers for nanomedical applications. Using the Bruggeman effective medium theory, resonant behavior of these nanoparticles is well described by including porosity of the core and shell, as well as surface defects, in the theoretical model. The theoretical model confirmed that there is a large amount of residual Ag in the HGNS, in order for them to be NIR resonant. In this study, the HGNS showed potential for photothermal therapy due to their stability when PEGylated under laser illumination on their plasmon resonance frequency, which corresponded well to the great potential previously shown in the literature. However, tracking the biodistribution of both component species, Ag and Au, from our HGNS following injection in mice strongly suggests that the nanoparticles are fragmenting after injection. Testing the HGNS@PEG stability over a large pH range and in serum at pH 7 showed that even when PEGylated, the nanoparticles fragment in low pH environments and in human serum at physiological pH. These early studies indicate that due to the remaining sacrificial Ag core, the loss of structural integrity, and the known toxicity of Ag, the stability and toxicity of HGNS made by galvanic replacements should be more carefully studied prior to their use in vivo. These results should strongly impact the assessment of ongoing efforts to design biocompatible plasmonic nanoparticles with compositions and structural properties appropriate for nanomedicine.

MATERIALS AND METHODS

Materials. Potassium carbonate and hydrogen tetrachloroaurate(III) trihydrate ($HAuCl_4 \cdot 3H_2O$) were purchased from Sigma Aldrich. Citrate-stabilized silver colloids (0.02 mg/mL)

of 40, 60, and 80 nm diameters were purchased from nanoComposix. Polyethylene glycol was purchased from Laysan Bio, Inc. Water was deionized and filtered by a Milli-Q water system (Millipore).

Synthesis and Functionalization of Hollow Gold Nanoshells. A 1% $HAuCl_4$ solution was made in H_2O (500 mL). A KCarb/Au solution was prepared by adding K_2CO_3 (0.025 g, 0.181 mmol) and 2 mL of 1% $HAuCl_4$ to 100 mL of H_2O, stirred for 30 min at room temperature, and left at 4 °C for an additional 30 min. For synthesis using 80 nm Ag cores, 24 mL of KCarb/Au was added to 72 mL of silver colloid under vigorous stirring. The solution was stirred for ∼2 min, then sonicated for 30 min. For synthesis using 40 and 60 nm silver cores, 24 mL of KCarb/Au was added to 72 mL of silver colloid under vigorous stirring. The solutions were stirred 30 min at 4 °C. All solutions were left at room temperature for a further 30 min to obtain the desired plasmon resonance. Solutions were centrifuged for 30 min at 800*g*. The 40 and 60 nm supernatant was centrifuged an additional 30 min at 800*g*. Particles were redispersed in H_2O.

HGNS were functionalized first with 10 000 MW thiol-mPEG and subsequently with 10 000 MW thiol-PEG-amine. A water bath was heated to 50 °C. A solution of HGNS was combined with thiol-PEG (15 μM final concentration) in a small vial and vortexed. The vial was floated in the water bath, covered with foil, and agitated in a Styrofoam box overnight. The solutions were centrifuged to remove excess PEG and redispersed in H_2O. The procedure was repeated with the HGNS functionalized with thiol-mPEG and a thiol-PEG-amine solution (70 μM final concentration) to achieve a mixed monolayer.

pH and Serum Studies. Aliquots of water were adjusted to various pH values from 2 to 12 using 0.1 M NaOH or 0.1 M HCl. The 82 nm HGNS and HGNS@PEG were centrifuged and redispersed into separate vials with varying pH. HGNS@PEG of 82 nm were centrifuged and redispersed into human serum AB obtained from Lonza. UV−vis measurements were obtained for each solution, to track the response of the plasmon resonance to the pH environments, and TEM images were taken to observe the integrity of the HGNS.

Irradiation with a NIR Laser. Solutions (2.5 mL) of each size of HGNS, bare and PEGylated, were diluted with H_2O to the same optical density. Extinction spectra and TEM images were obtained before resonant illumination. A solution was placed in a vial with a stir bar and thermocouple, and the vial was sealed with Parafilm. While stirring, the solution was irradiated with an 800 nm CW laser at 2.0 W/cm^2 for 25 min. Extinction spectra and TEM images were obtained from aliquots removed from the solution after irradiation.

***In Vivo* Studies.** The protocol for xenograft tumor creation and nude mice imaging was approved by the Institutional Animal Care and Use Committee (IACUC) of Baylor College of Medicine.

Athymic nude female mice (4−5 weeks old, Nude-Foxn1nu, Harlan Sprague−Dawley) were injected sc on the right flank with 1×10^6 U87_luc cells per mouse, in a total volume of 200 μL of serum-free medium. After 21−28 days, tumors grew to 8−12 mm in diameter and mice were randomized into 3 groups (*n* = 3).

Nanoparticles were administered *via* 200 μL tail vein injection with a concentration of 2×10^{11} particles/mL. Three different nanoparticles were injected, one particle type per group: HGNS@PEG 82 nm, HGNS@PEG 62 nm, and HGNS@PEG 43 nm.

To compare the biodistribution and the passive accumulation in the tumor by enhanced permeability and retention, all mice were euthanized with CO_2 asphyxiation 24 h after nanoparticle injection. The tumor, brain, heart, lung, liver, spleen, gut, and kidneys were collected, washed in phosphate-buffered saline, and then stored at −80 °C until analysis.

Inductively Coupled Plasma Mass Spectrometry. The organs were weighed into clean vials and digested in aqua regia for two days. After digestion, the samples were purified and all samples diluted in 10 mL of 1% aqua regia. The liver was diluted 100 times more, and the spleen was diluted 10 times more. The gold content was analyzed three times in the organs for statistical analysis. Subsequently, the silver content was analyzed three times in the organs. The ICP-MS analysis was performed using a Perkin-Elmer inductively coupled plasma mass spectrometer.

Instrumentation. Extinction spectra were measured on a Cary 5000 UV/vis/NIR spectrometer. Zeta potential measurements were taken with a Malvern Zetasizer Nano ZS. TEM images were obtained on a JEOL 2010 transmission electron microscope.

HRTEM was performed on a JEOL 2100 field emission gun transmission electron microscope. SEM images were taken on a FEI Quanta 650 at an accelerating voltage of 25 kV. XPS measurements were taken on a PHI Quantera X-ray photoelectron spectrometer.

REFERENCES AND NOTES

1. Bardhan, R.; Chen, W.; Bartels, M.; Perez-Torres, C.; Botero, M. F.; McAninch, R. W.; Contreras, A.; Schiff, R.; Pautler, R. G.; Halas, N. J.; *et al.* Tracking of Multimodal Therapeutic Nanocomplexes Targeting Breast Cancer *in Vivo*. *Nano Lett.* **2010**, *10*, 4920–4928.

2. Bardhan, R.; Chen, W.; Perez-Torres, C.; Bartels, M.; Huschka, R. M.; Zhao, L. L.; Morosan, E.; Pautler, R. G.; Joshi, A.; Halas, N. J. Nanoshells with Targeted Simultaneous Enhancement of Magnetic and Optical Imaging and Photothermal Therapeutic Response. *Adv. Funct. Mater.* **2009**, *19*, 3901–3909.

3. Bardhan, R. R.; Lal, S. S.; Joshi, A. A.; Halas, N. J. N. Theranostic Nanoshells: From Probe Design to Imaging and Treatment of Cancer. *Acc. Chem. Res.* **2011**, *44*, 936–946.

4. Weissleder, R. A Clearer Vision for *in Vivo* Imaging. *Nat. Biotechnol.* **2001**, *19*, 316–317.

5. Hirsch, L. R.; Stafford, R. J.; Bankson, J. A.; Sershen, S. R.; Rivera, B.; Price, R. E.; Hazle, J. D.; Halas, N. J.; West, J. L. Nanoshell-Mediated Near-Infrared Thermal Therapy of Tumors under Magnetic Resonance Guidance. *Proc. Natl. Acad. Sci. U.S.A.* **2003**, *100*, 13549–13554.

6. O'Neal, D. P.; Hirsch, L. R.; Halas, N. J.; Payne, J. D.; West, J. L. Photo-Thermal Tumor Ablation in Mice Using Near Infrared-Absorbing Nanoparticles. *Cancer Lett.* **2004**, *209*, 171–176.

7. Dickerson, E. B.; Dreaden, E. C.; Huang, X.; El-Sayed, I. H.; Chu, H.; Pushpanketh, S.; McDonald, J. F.; El-Sayed, M. A. Gold Nanorod Assisted Near-Infrared Plasmonic Photothermal Therapy (PPTT) of Squamous Cell Carcinoma in Mice. *Cancer Lett.* **2008**, *269*, 57–66.

8. Goodrich, G. P.; Bao, L.; Gill-Sharp, K.; Sang, K. L.; Wang, J.; Payne, J. D. Photothermal Therapy in a Murine Colon Cancer Model Using Near-Infrared Absorbing Gold Nanorods. *J. Biomed. Opt.* **2010**, *15*, 018001.

9. Huang, X.; El-Sayed, I. H.; Qian, W.; El-Sayed, M. A. Cancer Cell Imaging and Photothermal Therapy in the Near-Infrared Region by Using Gold Nanorods. *J. Am. Chem. Soc.* **2006**, *128*, 2115–2120.

ARTICLE

10. Van de Broek, B.; Devoogdt, N.; D'Hollander, A.; Gijs, H.-L.; Jans, K.; Lagae, L.; Muyldermans, S.; Maes, G.; Borghs, G. Specific Cell Targeting with Nanobody Conjugated Branched Gold Nanoparticles for Photothermal Therapy. *ACS Nano* **2011**, *5*, 4319–4328.

11. Wang, Y.; Black, K. C. L.; Luehmann, H.; Li, W.; Zhang, Y.; Cai, X.; Wan, D.; Liu, S.-Y.; Li, M.; Kim, P.; *et al.* Comparison Study of Gold Nanohexapods, Nanorods, and Nanocages for Photothermal Cancer Treatment. *ACS Nano* **2013**, *7*, 2068–2077.

12. Chen, J.; Wang, D.; Xi, J.; Au, L.; Siekkinen, A.; Warsen, A.; Li, Z.-Y.; Zhang, H.; Xia, Y.; Li, X. Immuno Gold Nanocages with Tailored Optical Properties for Targeted Photothermal Destruction of Cancer Cells. *Nano Lett.* **2007**, *7*, 1318–1322.

13. Chen, W.; Bardhan, R.; Bartels, M.; Perez-Torres, C.; Pautler, R. G.; Halas, N. J.; Joshi, A. A Molecularly Targeted Theranostic Probe for Ovarian Cancer. *Mol. Cancer Ther.* **2010**, *9*, 1028–1038.

14. Melancon, M. P.; Lu, W.; Yang, Z.; Zhang, R.; Cheng, Z.; Elliot, A. M.; Stafford, J.; Olson, T.; Zhang, J. Z.; Li, C. *In Vitro* and *in Vivo* Targeting of Hollow Gold Nanoshells Directed at Epidermal Growth Factor Receptor for Photothermal Ablation Therapy. *Mol. Cancer Ther.* **2008**, *7*, 1730–1739.

15. Lu, W.; Melancon, M. P.; Xiong, C.; Huang, Q.; Elliott, A.; Song, S.; Zhang, R.; Flores, L. G.; Gelovani, J. G.; Wang, L. V.; *et al.* Effects of Photoacoustic Imaging and Photothermal Ablation Therapy Mediated by Targeted HAuNS in an Orthotopic Mouse Xenograft Model of Glioma. *Cancer Res.* **2011**, *71*, 6116–6121.

16. Wang, S.-H.; Lee, C.-W.; Chiou, A.; Wei, P.-K. Size-Dependent Endocytosis of Gold Nanoparticles Studied by Three-Dimensional Mapping of Plasmonic Scattering Images. *J. Nanobiotechnol.* **2010**, *8*, 33.

17. Rao, J. Shedding Light on Tumors Using Nanoparticles. *ACS Nano* **2008**, *2*, 1984–1986.

18. Chen, J.; Glaus, C.; Laforest, R.; Zhang, Q.; Yang, M.; Gidding, M.; Welch, M. J.; Xia, Y. Gold Nanocages as Photothermal Transducers for Cancer Treatment. *Small* **2010**, *6*, 811–817.

19. An, K.; Hyeon, T. Synthesis and Biomedical Applications of Hollow Nanostructures. *Nano Today* **2009**, *4*, 359–373.

20. Choi, Y.; Hong, S.; Liu, L.; Kim, S. K.; Park, S. Galvanically Replaced Hollow Au-Ag Nanospheres: Study of Their Surface Plasmon Resonance. *Langmuir* **2012**, 6670–6676.

21. Lu, X.; Chen, J.; Skrabalak, S. E.; Xia, Y. Galvanic Replacement Reaction: A Simple and Powerful Route to Hollow and Porous Metal Nanostructures. *Proc. Inst. Mech. Eng., Part N* **2008**, *221*, 1–16.

22. Preciado-Flores, S.; Wang, D.; Wheeler, D. A.; Newhouse, R.; Hensel, J. K.; Schwartzberg, A.; Wang, L.; Zhu, J.; Barboza-Flores, M.; Zhang, J. Z. Highly Reproducible Synthesis of Hollow Gold Nanospheres with Near Infrared Surface Plasmon Absorption Using PVP as Stabilizing Agent. *J. Mater. Chem.* **2011**, *21*, 2344–2350.

23. Schwartzberg, A. M.; Olson, T. Y.; Talley, C. E.; Zhang, J. Z. Synthesis, Characterization, and Tunable Optical Properties of Hollow Gold Nanospheres. *J. Phys. Chem. B* **2006**, *110*, 19935–19944.

24. Sun, Y.; Xia, Y. Mechanistic Study on the Replacement Reaction between Silver Nanostructures and Chloroauric Acid in Aqueous Medium. *J. Am. Chem. Soc.* **2004**, *126*, 3892–3901.

25. Vongsavat, V. V.; Vittur, B. M. B.; Bryan, W. W. W.; Kim, J.-H. J.; Lee, T. R. T. Ultrasmall Hollow Gold-Silver Nanoshells with Extinctions Strongly Red-Shifted to the Near-Infrared. *ACS Appl. Mater. Interfaces* **2011**, *3*, 3616–3624.

26. Zhang, K.; Holloway, T.; Wingfield, A.; Pradhan, J.; Cao, W.; Pradhan, A. K. Hollow Gold Nanospheres: Growth, Morphology, Composition and Absorption Characteristics. *Micro Nanosyst.* **2011**, *3*, 76–82.

27. Sun, Y.; Mayers, B. T.; Xia, Y. Template-Engaged Replacement Reaction: A One-Step Approach to the Large-Scale Synthesis of Metal Nanostructures with Hollow Interiors. *Nano Lett.* **2002**, *2*, 481–485.

28. Wang, W.; Dahl, M.; Yin, Y. Hollow Nanocrystals through the Nanoscale Kirkendall Effect. *Chem. Mater.* **2012**, *25*, 1179–1189.

29. Schwartzberg, A. M.; Olson, T. Y.; Talley, C. E.; Zhang, J. Z. Gold Nanotubes Synthesized *via* Magnetic Alignment of Cobalt Nanoparticles as Templates. *J. Phys. Chem. C* **2007**, *111*, 16080–16082.

30. Olson, T. Y.; Schwartzberg, A. M.; Orme, C. A.; Talley, C. E.; O'Connell, B.; Zhang, J. Z. Hollow Gold–Silver Double-Shell Nanospheres: Structure, Optical Absorption, and Surface-Enhanced Raman Scattering. *J. Phys. Chem. C* **2008**, *112*, 6319–6329.

31. Zhang, J. Z. Biomedical Applications of Shape-Controlled Plasmonic Nanostructures: A Case Study of Hollow Gold Nanospheres for Photothermal Ablation Therapy of Cancer. *J. Phys. Chem. Lett.* **2010**, *1*, 686–695.

32. Melancon, M. P.; Elliott, A.; Ji, X.; Shetty, A.; Yang, Z.; Tian, M.; Taylor, B.; Stafford, R. J.; Li, C. Theranostics with Multifunctional Magnetic Gold Nanoshells: Photothermal Therapy and T2* Magnetic Resonance Imaging. *Invest. Radiol.* **2011**, *46*, 132–140.

33. Melancon, M. P.; Lu, W.; Zhong, M.; Zhou, M.; Liang, G.; Elliott, A. M.; Hazle, J. D.; Myers, J. N.; Li, C.; Stafford, R. J. Targeted Multifunctional Gold-Based Nanoshells for Magnetic Resonance-Guided Laser Ablation of Head and Neck Cancer. *Biomaterials* **2011**, *32*, 7600–7608.

34. You, J.; Zhang, G.; Li, C. Exceptionally High Payload of Doxorubicin in Hollow Gold Nanospheres for Near-Infrared Light-Triggered Drug Release. *ACS Nano* **2010**, *4*, 1033–1041.

35. You, J.; Shao, R.; Wei, X.; Gupta, S.; Li, C. Near-Infrared Light Triggers Release of Paclitaxel from Biodegradable Microspheres: Photothermal Effect and Enhanced Antitumor Activity. *Small* **2010**, *6*, 1022–1031.

36. Sun, Y.; Xia, Y. Alloying and Dealloying Processes Involved in the Preparation of Metal Nanoshells through a Galvanic Replacement Reaction. *Nano Lett.* **2003**, *3*, 1569–1572.

37. Johnson, P. B.; Christy, R. W. Optical Constants of the Noble Metals. *Phys. Rev. B* **1972**, *6*, 4370.

38. Zeng, X.; Bergman, D.; Hui, P.; Stroud, D. Effective-Medium Theory for Weakly Nonlinear Composites. *Phys. Rev. B: Condens. Matter Mater. Phys.* **1988**, *38*, 10970–10973.

39. Shi, Z.; Piredda, G.; Liapis, A. C.; Nelson, M. A.; Novotny, L.; Boyd, R. W. Surface-Plasmon Polaritons on Metal-Dielectric Nanocomposite Film. *Opt. Lett.* **2009**, *34*, 3535–3537.

40. Bruggeman, V. D. Berechnung Verschiedener Physikalischer Konstanten von Heterogenen Substanzen. I. Dielektrizitätskonstanten und Leitfähigkeiten der Mischkörper aus Isotropen Substanzen. *Ann. Phys. (Berlin, Ger.)* **1935**, *416*, 636–664.

41. Choy, T. C. *Effective Medium Theory: Principles and Applications*; Oxford University Press on Demand, 1999; Vol. 102.

42. Lipka, J.; Semmler-Behnke, M.; Sperling, R. A.; Wenk, A.; Takenaka, S.; Schleh, C.; Kissel, T.; Parak, W. J.; Kreyling, W. G. Biodistribution of PEG-Modified Gold Nanoparticles Following Intratracheal Instillation and Intravenous Injection. *Biomaterials* **2010**, *31*, 6574–6581.

43. Gomes-da-Silva, L. C.; Fonseca, N. A.; Moura, V.; Pedroso de Lima, M. C.; Simões, S.; Moreira, J. N. Lipid-Based Nanoparticles for siRNA Delivery in Cancer Therapy: Paradigms and Challenges. *Acc. Chem. Res.* **2012**, *45*, 1163–1171.

44. Wang, Y.; Liu, Y.; Luehmann, H.; Xia, X.; Brown, P.; Jarreau, C.; Welch, M.; Xia, Y. Evaluating the Pharmacokinetics and *in Vivo* Cancer Targeting Capability of Au Nanocages by Positron Emission Tomography Imaging. *ACS Nano* **2012**, *6*, 5880–5888.

45. Xie, H.; Wang, Z. J.; Bao, A.; Goins, B.; Phillips, W. T. *In Vivo* PET Imaging and Biodistribution of Radiolabeled Gold Nanoshells in Rats with Tumor Xenografts. *Int. J. Pharm.* **2010**, *395*, 324–330.

46. Johnston, H. J.; Hutchison, G.; Christensen, F. M.; Peters, S.; Hankin, S.; Stone, V. A Review of the *in Vivo* and *in Vitro* Toxicity of Silver and Gold Particulates: Particle Attributes and Biological Mechanisms Responsible for the Observed Toxicity. *Crit. Rev. Toxicol.* **2010**, *40*, 328–346.

47. Kittler, S.; Greulich, C.; Diendorf, J.; Koller, M.; Epple, M. Toxicity of Silver Nanoparticles Increases during Storage Because of Slow Dissolution Under Release of Silver Ions. *Chem. Mater.* **2010**, *22*, 4548–4554.

48. Xiu, Z.-M.; Zhang, Q.-B.; Puppala, H. L.; Colvin, V. L.; Alvarez, P. J. J. Negligible Particle-Specific Antibacterial Activity of Silver Nanoparticles. *Nano Lett.* **2012**, *12*, 4271–4275.

49. Liu, J.; Wang, Z.; Liu, F. D.; Kane, A. B.; Hurt, R. H. Chemical Transformations of Nanosilver in Biological Environments. *ACS Nano* **2012**, *6*, 9887–9899.

50. Issaq, H. J.; Xiao, Z.; Veenstra, T. D. Serum and Plasma Proteins. *Chem. Rev.* **2007**, *107*, 3601–3620.

51. Schaller, J.; Gerber, S.; Kaempfer, U.; Lejon, S.; Trachsel, C. Blood Components. In *Human Blood Plasma Proteins: Structure and Function*, 1st ed.; John Wiley & Sons, Inc.: Chichester, England, 2008.

52. Reidy, B.; Hasse, A.; Luch, A.; Dawson, K. A.; Lynch, I. Mechanisms of Silver Nanoparticle Release, Transformation and Toxicity: A Critical Review of Current Knowledge and Recommendations for Future Studies and Applications. *Materials* **2013**, *6*, 2295–2350.

53. Lok, C.-N.; Ho, C.-M.; Chen, R.; He, Q.-Y.; Yu, W.-Y.; Sun, H.; Tam, P. K.-H.; Chiu, J.-F.; Che, C.-M. Silver Nanoparticles: Partial Oxidation and Antibacterial Activities. *J. Biol. Inorg. Chem.* **2007**, *12*, 527–534.

54. Bouwmeester, H.; Poortman, J.; Peters, R. J.; Wijma, E.; Kramer, E.; Makama, S.; Puspitaninganindita, K.; Marvin, H. J. P.; Peijnenburg, A. A. C. M.; Hendriksen, P. J. M. Characterization of Translocation of Silver Nanoparticles and Effects on Whole-Genome Gene Expression Using an *in Vitro* Intestinal Epithelium Coculture Model. *ACS Nano* **2011**, *5*, 4091–4103.

55. Stebounova, L. V.; Guio, E.; Grassian, V. H. Silver Nanoparticles in Simulated Biological Media: A Study of Aggregation, Sedimentation, and Dissolution. *J. Nanopart. Res.* **2011**, *13*, 233–244.

56. Liu, J.; Hurt, R. H. Ion Release Kinetics and Particle Persistence in Aqueous Nano-Silver Colloids. *Environ. Sci. Technol.* **2010**, *44*, 2169–2175.

57. Lynch, I.; Dawson, K. A. Protein-Nanoparticle Interactions. *Nano Today* **2008**, *3*, 40–47.

58. Muthusamy, B.; Hanumanthu, G.; Suresh, S.; Rekha, B.; Srinivas, D.; Karthick, L.; Vrushabendra, B. M.; Sharma, S.; Mishra, G.; Chatterjee, P.; *et al.* Plasma Proteome Database as a Resource for Proteomics Research. *Proteomics* **2005**, *5*, 3531–3536.